Observation of inertia-gravity wave attractors in an axisymmetric enclosed basin

Corentin Pacary, Thierry Dauxois, Evgeny Ermanyuk, Pascal Metz, Marc Moulin, Sylvain Joubaud

Editors' Suggestion

Observation of inertia-gravity wave attractors in an axisymmetric enclosed basin

Corentin Pacary,[1] Thierry Dauxois,[1] Evgeny Ermanyuk,[2] Pascal Metz,[1] Marc Moulin,[1] and Sylvain Joubaud[1,3]

[1]*ENS de Lyon, CNRS, Laboratoire de Physique, F-69342 Lyon, France*
[2]*Lavrentyev Institute of Hydrodynamics, av. Lavrentyev 15, Novosibirsk 630090, Russia*
[3]*Institut Universitaire de France (IUF), 1 rue Descartes, 75005 Paris, France*

(Received 6 March 2023; accepted 12 September 2023; published 25 October 2023)

Internal waves are ubiquitous in the ocean and play an essential role in the transport of energy and mixing. Their peculiar reflection enables the concentration of energy on a limit cycle. With wave beams viewed as rays, this reflection on an inclined slope shrinks its width and generically brings closer two initially different trajectories eventually reaching a limit cycle called an attractor. Following previous studies, a ray-tracing algorithm is used to track the convergence of wave beams onto such a structure in a 3D axisymmetric domain. This information is used to design experiments using a truncated conical shaped tank in order to form an inertia-gravity waves attractor in a 3D axisymmetric geometry. By increasing the amplitude of the forcing, an evolution of the attractor characteristics can be observed. The occurrence of waves at frequencies lower than the forcing frequency ω_0 suggests triadic resonant instability in a rotating or in a stratified case. Experiments performed in a stratification-only or a rotation-only case indicate two distinct behaviors. The existence of easily excited standing waves, resonant modes of the tank, at frequencies lower than the forcing one enables sharp triadic resonance instability for internal gravity waves, which is not possible for inertial waves. The effect of the symmetry axis is also investigated by adding a cylinder of sufficient diameter at the center of the domain for the wave to reflect on and thereby avoid the interaction on the singularity. Without it, the large amplitude of the waves on the axis triggers nonlinear effects and mixing, denying the access to the wave turbulence regime.

DOI: 10.1103/PhysRevFluids.8.104802

I. INTRODUCTION

Inertia-gravity waves exist in stratified rotating fluids. In the ocean, internal waves are generated by the interaction of the tides with topography [1]. Globally, a third of the kinetic energy is dissipated in the near field [2], and two thirds travel long distances [3]. Such waves propagate until they break or are totally damped, causing transfer of energy between scales and mixing [4,5]. Such phenomena are crucial for the energy budget of the oceans [6,7]. While internal waves mostly propagate as modes (or internal tides) in the oceanographic context [8], wave beams are also observed [9], and they can be more convenient to probe some properties of internal gravity waves [10]. In the laboratory, a stably stratified fluid of density $\rho(z)$ rotating at a frequency Ω can exhibit internal waves when excited at frequency ω_0 that will propagate at an angle θ with the vertical (the gravity $\mathbf{g} = -g\mathbf{e}_z$ and the rotation $\mathbf{\Omega} = \Omega\mathbf{e}_z$ being aligned along this axis), verifying the dispersion relation

$$\omega_0^2 = N^2 \sin^2\theta + f_c^2 \cos^2\theta \tag{1}$$

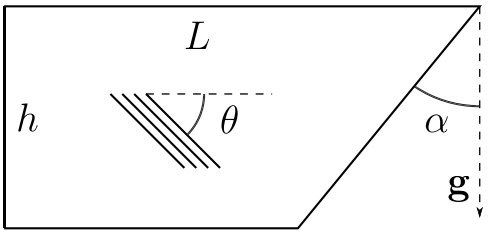

FIG. 1. 2D trapezoid of height h, length L, and slope angle α with respect to the gravity g, and an inertia-gravity wave with a group velocity making an angle θ with respect to the horizontal.

with $f_c = 2\Omega$ the Coriolis parameter and $N^2 = -(g/\rho_0)\frac{\mathrm{d}\rho}{\mathrm{d}z}$ the square of the buoyancy frequency with ρ_0 a density reference and g the norm of the gravitational field. In this article, the stratification will be considered as linear $N(z) = N_0$. Inertia-gravity waves propagate only if $\min(f_c, N) < \omega_0 < \max(f_c, N)$. We call them internal gravity waves when $f_c = 0$ and inertial waves when $N = 0$.

In a linearly stratified fluid and/or a rotating fluid, inertia-gravity waves propagate at a fixed angle with the vertical. Consequently, unlike electromagnetic waves, they do not obey the Snell-Descartes laws of reflection, causing the focusing (or defocusing) of a wave beam at the reflection on an inclined (not horizontal nor vertical) slope [11,12]. At a reflection on a slope making an angle α to the vertical, the wave beam width is modified by a factor

$$\gamma = \left|\frac{\cos(\theta - \alpha)}{\cos(\theta + \alpha)}\right|. \tag{2}$$

Now thinking about the trajectory of the wave beam, or ray [13], an inclined slope can bring closer two trajectories, suggesting a dynamical system approach. In the case of a closed domain, in a 2D trapezoid or in a paraboloid, consecutive focusing reflections may lead to a closed orbit, limit cycle for any initial condition called an attractor [14]. In a trapezoidal domain of height h, length L, and slope angle α (see Fig. 1), an internal wave beam propagating at an angle θ can be simply described by a geometrical problem with two nondimensional parameters $d = 1 - (2h/L)\tan\alpha$ and $\tau = (2h/L)\sqrt{1/\sin^2\theta - 1}$ that predict if a limit cycle exists [15–17]. In three dimensions, the reflection of an internal wave beam occurs on a cone; Pillet *et al.* [18] have thoroughly calculated the formula for a 3D reflection and applied their results on a Cartesian 3D geometry with an invariance property. The symmetry breaking showed the possibility of a true, localized attractor in three dimensions [19]. Other studies in three dimensions have considered the formation of attractors and normal modes in spheres and/or spherical shells [20–22], relevant to astrophysics. It is still debated whether such a structure can be found in the ocean [23–25], but experimentally, the attractor helps to reach nonlinear regimes by increasing the energy density via the focusing reflections. As such, they have been used as tools to study triadic resonant instability (TRI) and try to reach the weakly nonlinear regime of wave turbulence [26]. Most of those experiments have been done in two dimensions [27,28], while 3D experiments [29–32] on wave turbulence did not use attractors. One recent exception is the study of the formation of attractors in an annulus with a conical bottom [33,34]. Previously, the propagation of inertial modes in a cone had been observed [35] and computed numerically [36]. In the present paper, we study experimentally the existence of 2D attractors in an axisymmetric setup and check on the differences with the 2D trapezoid case. We show that inertial and internal gravity waves behave differently in this particular setup.

In Sec. II we present the experimental setup and the analysis of the problem. We then exhibit the formation of attractor in Sec. III A and their articulation with standing waves in Sec. III B. Section III C shows how TRI occurs in this experimental setup, and the effect of the rotation axis is discussed in Sec. III D. Section IV concludes the paper.

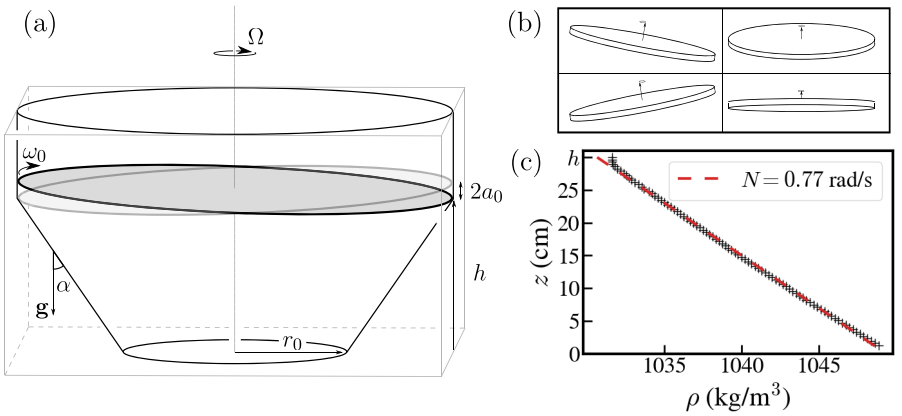

FIG. 2. (a) Sketch of the experimental setup. (b) Decomposition of the movement of the forcing plate, from left to right, top to bottom. (c) Data points in black (one every ten is represented) and linear fit in dashed red of density as a function of height.

II. SETUP AND METHODS

A. Experimental setup

A sketch of the experimental setup is presented in Fig. 2. A conical frustum of radius $r_0 = 268 \pm 2\,\text{mm}$ and side angle $\alpha = 30 \pm 1^\circ$ is filled up to $h = 31 \pm 1\,\text{cm}$ with water at room temperature. Salt and two controlled pumps have been used to obtain a constant stable stratification $N(z) = N$; an example is given in Fig. 2(c). An adapted double-bucket method similar to [37,38] has to be used as the horizontal section of the tank is not constant. The density profile is measured with a calibrated conductivity-temperature probe. To limit optical deformations due to the cone curvature, this tank is placed within a square-bottom tank of dimension $L \times L \times H = 900\,\text{mm} \times 900\,\text{mm} \times 450\,\text{mm}$ filled with freshwater at density ρ_0. The whole setup is mounted on a rotating table slowly put into rotation to avoid mixing [39].

The velocity field is measured with PIV. Two lasers, turquoise 488 nm and green 532 nm, illuminate 10 μm hollow glass spheres of density 1.1 and 10 μm silver-coated hollow glass spheres of density 1.4 (Dantec) along two perpendicular planes: the vertical one $(\hat{x}, \hat{z})$ going through the center, and the horizontal one $(\hat{x}, \hat{y})$. Silver-coated particles, more reflective, are needed for the visualization of the horizontal plane with a bigger area than the vertical one. The horizontal sheet, whose height can be set with a vertical translation stage, is viewed from the side thanks to a 45° mirror. Through interference filters to block the other laser's light, two cameras record images which are then treated with the UVMAT software [40] to obtain the velocity fields $v_x(x, y, t)$ and $v_y(x, y, t)$ in an horizontal plane at $z = z_0$, or $v_x(x, z, t)$ and $v_z(x, z, t)$ in a vertical plane at $y = 0$.

Energy is injected into the system by a moving plexiglass plate of the same radius as the top base of the cone $R_h = R(h) = 440 \pm 2\,\text{mm}$. Two pistons 90° apart and in phase quadrature give the plate a precession movement as depicted in Fig. 2(b). Using cylindrical coordinates at position $z = 0$ (r, φ), the movement of the plate is described by

$$a = a_0(r/R_h)\cos(\omega_0 t - m\varphi), \tag{3}$$

with $m = -1$ the azimuthal wave number, ω_0 the forcing frequency, and a_0 the amplitude of the forcing. The plate precession is clockwise (note that in Fig. 2, the rotation is clockwise when viewed from the top). The plate is not parallel to the fluid surface and is slightly immersed in the experiments shown in this paper. A closely related way of forcing inertial waves was used in the 1970s [41]. In a nonrotating homogeneous experiment ($N = 0$ and $\Omega = 0$), the generated velocity field can be compared to a rotating seiche mode. At any given time t, it is composed of two movements:

TABLE I. Experimental parameters: N the buoyancy frequency, $f_c = 2\Omega$ the Coriolis parameter (positive values are clockwise rotations, negative are anticlockwise), θ the angle of propagation tuned by the forcing frequency, and a_0 the amplitude of the forcing.

Experiment	N (rads^{-1})	f_c (rads^{-1})	$\sin\theta$	a_0(mm)
A	0.0	0.0	–	0, 2, 4, 5, 8, 9, 10
B	0.0	±1.052	0.31, 0.64, 0.66, 0.68, 0.7, 0.72, 0.75, 0.79, 0.85, 0.92	1, 2, 3, 5, 6, 8, 9, 10
C	0.0	−0.838	0.64	0, 1, 2, 3, 5, 10
D	0.0	−0.838	Impulse	10
E	0.63–0.81	0.0	0.32,0.49, 0.57, 0.6, 0.64, 0.74, 0.82, 1.5	1, 2, 3, 4, 5, 6, 7, 8, 9, 10
F	1.031	0.0	0.48, 0.61–0.68, 0.72, 0.84	1
G	0.73	0.0	Impulse	10
H	0.77	0.0	0.64	Increase from 0 to 10
I	0.78	0.040	0.64, 0.61	1, 2
J	0.76	0.076	0.55, 0.61, 0.64	0, 2, 4, 5, 6, 8
K	0.76	0.152	0.60, 0.63, 0.80	0, 2, 4, 6, 9, 10
L	0.78	−0.392	0.85, 0.61, 0.41, 0.22	2, 6, 9
M	0.78	−1.566	0.69, 1.1	1, 2
N	1.031	0.344	0.58, 0.64–0.68	1, 3, 6, 9

a horizontal one with fluid going from the point where $a = -a_0$ to the point where $a = a_0$ and a vertical one with fluid going down in one half of the tank (at the points near $a = -a_0$) and up in the other half. In experiments where either N, Ω or both are nonzero, the vertical movement imposed by the forcing and the lateral slope gives birth to waves. Table I presents the different parameters (N, f_c, $\sin\theta$, and a_0) used in the experiments.

B. Ray tracing

The experimental setup was built as an axisymmetric version of the usual trapezoidal tank generating attractors to study dissipation of energy or nonlinear effects in a 3D domain. The method to reach the nonlinear regimes relied on the geometric focusing and the geometric formation of attractors with clues, but no proof that such mechanisms would hold in three dimensions [18,34]. To understand 3D propagation, in addition to experiments, it is possible to develop an algorithm simulating the propagation of a wave beam in a confined domain. Considering the geometry of the experimental setup, one could expect an axisymmetric structure. A first step is to study the propagation in a plane containing the axis of symmetry. This comes back to consider the 2D trapezoid as in [14]. With constant N and/or f_c, a wave beam is represented as a ray, which is a straight line making an angle θ with the horizontal.

In two dimensions, a ray is defined by its direction, a velocity $\mathbf{v} = (v_x, v_z)$. A superscript i, respectively r, denotes the incident ray with respect to a reflection, respectively, the reflected ray.

The ray-tracing algorithm is then build as straightforwardly as possible: from an initial condition, it computes the intersection of the ray and the boundaries and imposes the boundary conditions ($v_x^r = -v_x^i$ at $x = 0$, $v_{z,}^r = -v_z^i$ at $z = 0$ and $z = h$, $v_x^r = -v_x^i$ if the reflection is subcritical on the slope, or $v_z^r = -v_z^i$ if the reflection is super-critical). From two close initial conditions separated initially by a distance e_0, the distance e between two trajectories can be followed as a function of time, and the Lyapunov exponent λ defined as $e = e_0 \exp(-\lambda n)$, with n the number of reflections, is computed. Repeated for 1024×1024 values of (d, τ) as shown Fig. 3(a), this basic algorithm that does not enforce the geometric focusing explicitly exhibits the same features as in [15]. The bottom left of the diagram is the zone of point attractors [supercritical reflections on the slope lead all the

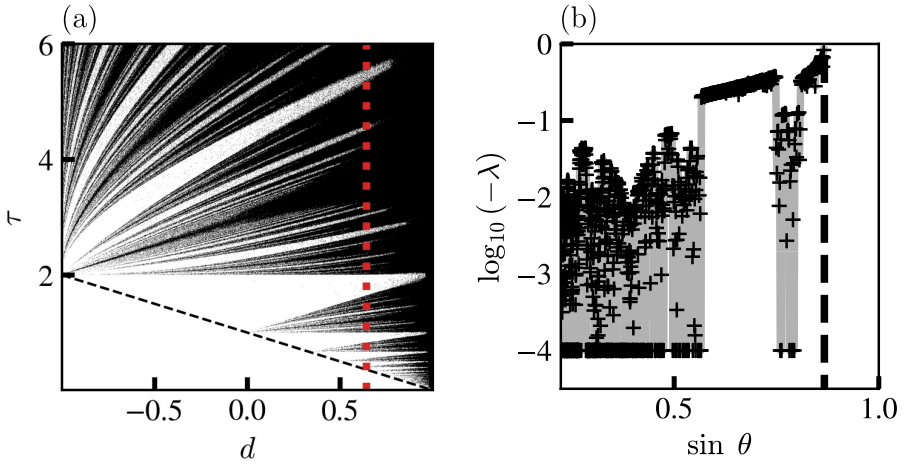

FIG. 3. (a) Lyapunov exponent for 2D trajectories as a function of the parameters (d, τ). Each pixel is either white or black if the Lyapunov exponent is larger (resp. lower) than -2, indicating short, quickly converging attractors (resp. long, slowly converging). The red dashed line is the value of d fixed by the setup's geometry. (b) Values of the Lyapunov exponent λ along the red dashed line in the (d, τ) diagram. Each point is a numerical computation; the minimum value of λ has been set to -4 for visualization purposes. In both figures, the black dashed line is the critical reflection ($\theta = \alpha$).

rays to a corner of the domain, at coordinates (R_h, h)], and the rest of the diagram is composed of Arnold tongues in white corresponding to short closed orbits and quick focusing attractors. In the experiments described in this paper, the geometric parameters (L, h, α) of the tank are fixed, with only θ varying, corresponding to a cut at $d = 0.217$ in Fig. 3(a). The variation of the Lyapunov exponent λ along this cut is represented in Fig. 3(b); it indicates two main zones where attractors can be expected:

(1) $0.582 < \sin\theta < 0.748$: (1,1) attractors, the ones with the shorter perimeter with only one reflection on the top and one on the slope

(2) $0.809 < \sin\theta < 0.867$: (2,1) attractors, with two reflections on the top and one on the slope

Those two zones are therefore the ones targeted in the experiments as shown in Table I. One could argue that they should be named (2,2) and (4,2) if we stick to the strict definition given in [14]. Considering the symmetry of the domain, we chose to name the attractor as their 2D-trapezoid counterpart. This is possible because, with the geometry of this basin, only attractors with an even number of reflection at the top or bottom boundary are possible. When the number is odd, focusing at one sloping wall is compensated by defocusing at the opposite wall. It is a neutrally stable case, with a Lyapunov exponent of zero.

This reasoning has been done in a vertical plane containing the symmetry axis, but out-of-plane rays are still to be considered.

Using the properties of reflections of inertia-gravity waves in three dimensions introduced earlier, one could expect that in the axisymmetric case any ray will align with a diameter of the cone as the gradient of the slope is always directed radially. To verify this property numerically, the previous algorithm has been adapted to a propagation inside a 3D domain taking into account new boundary conditions. A xy projection of the situation is represented in Fig. 4; quantities at the reflection n have an index n and a superscript i (respectively r) for "incident" before the reflection (resp. "reflected," after the reflection). At $z = 0$ and $z = h$, $v^r_{z,n} = -v^i_{z,n}$, and using the formula proposed in [18,42] for the reflection on the slope

$$v'^r_{x,n} = \frac{(1+s^2)v'^i_{x,n} - 2\frac{s}{\tan(\theta)}v'^i_{z,n}}{1-s^2}, \tag{4}$$

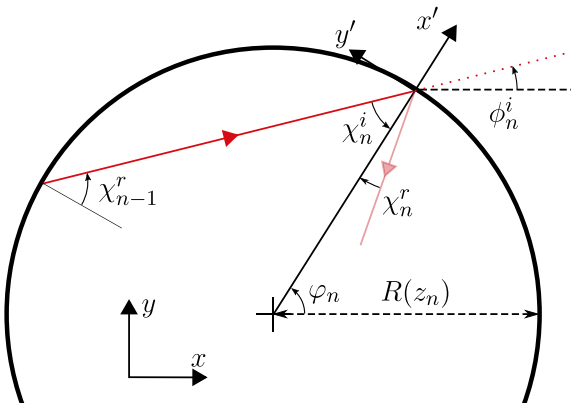

FIG. 4. Scheme of a reflection projected horizontally (top view). Φ is the horizontal direction of the ray, φ the azimuthal position of the reflection, and $R(z)$ the radius of the cone at the reflection height. n is the number of reflections on the slope, and i stands for incident ray and r for reflected.

$$v'^{r}_{y,n} = v'^{i}_{y,n}, \tag{5}$$

$$v'^{r}_{z,n} = \frac{-(1+s^2)v'^{i}_{z,n} + 2s\tan(\theta)v'^{i}_{x,n}}{1-s^2}, \tag{6}$$

with $\mathbf{v}' = (v'_x, v'_y, v'_z)$ the velocity field in the rotated frame of reference such that $(\mathbf{e}'_\mathbf{x}, \mathbf{e}'_\mathbf{y}) = (\mathbf{e}_\mathbf{r}, \mathbf{e}_\varphi)$ at the reflection point and $s = \tan\alpha/\tan\theta$. Figures 5(a) and 5(b) show projections in the xy and xz planes of a trajectory with parameters

$$(x_0, y_0, z_0, \sin\theta, \phi_0) = (0,\ 0.93r_0,\ 2h/3,\ 0.61,\ 50^\circ) \tag{7}$$

with ϕ the azimuthal direction of the ray defined by $\cos\phi = v_x/\sqrt{v_x^2+v_y^2}$. With this set of parameters, a clear convergence can be seen to an attractor composed of two (1,1) attractors in a vertical plane passing through the revolution axis of the cone. A quantitative way to measure the convergence to a plane is to look at the evolution of χ, the angle between the direction of the ray and the diameter of the circle, as a function of the number of slope reflections n, a bottom or a top reflection being neutral.

A naive model would be a geometric evolution of χ in the local frame of the reflection with a coefficient γ_ϕ such that $\phi_n^r - \varphi_n = \chi_n^r = \gamma_\phi \chi_n^i$, with φ the azimuthal coordinate of the reflection point (see Fig. 4). In a cone, two successive reflection angles are related by $R(z_{n+1})\cos\chi_{n+1}^i = R(z_n)\cos\chi_n^r$, with $R(z_n)$ the radius at the reflection point. With a sufficient number of reflections randomly distributed those factors should compensate, and we will consider that $\chi_{n+1}^i = \chi_n^r$ and so

$$\chi_n = \gamma_\phi^n \chi_0, \tag{8}$$

with n the number of focusing reflections. Finally,

$$\Delta\chi_n = \chi_n^r - \chi_n^i = (1-\gamma_\phi)\gamma_\phi^{n-1}\chi_0. \tag{9}$$

According to this model, with $|\gamma_\phi| < 1$ the ray tends toward a diameter ($\chi = 0$) with an exponential decay of rate $\Lambda_\phi = \ln\gamma_\phi$.

Figure 6(a) is a semilogarithmic plot of $\Delta\chi$ with the same parameters as above and varying ϕ_0. It displays a clear exponential decay. On the contrary, in the case $\sin\theta = 0.292$ represented in Fig. 6(b), no convergence is observed, and different behaviors are observed depending on ϕ_0.

To investigate further the effect of θ, we computed Λ_ϕ for 1000×90 values of $(\sin\theta, \phi_0)$. Figure 7(b) presents $\log\Lambda_\phi$ as a function of $\sin\theta$ and ϕ_0. Values closer to zero correspond to faster

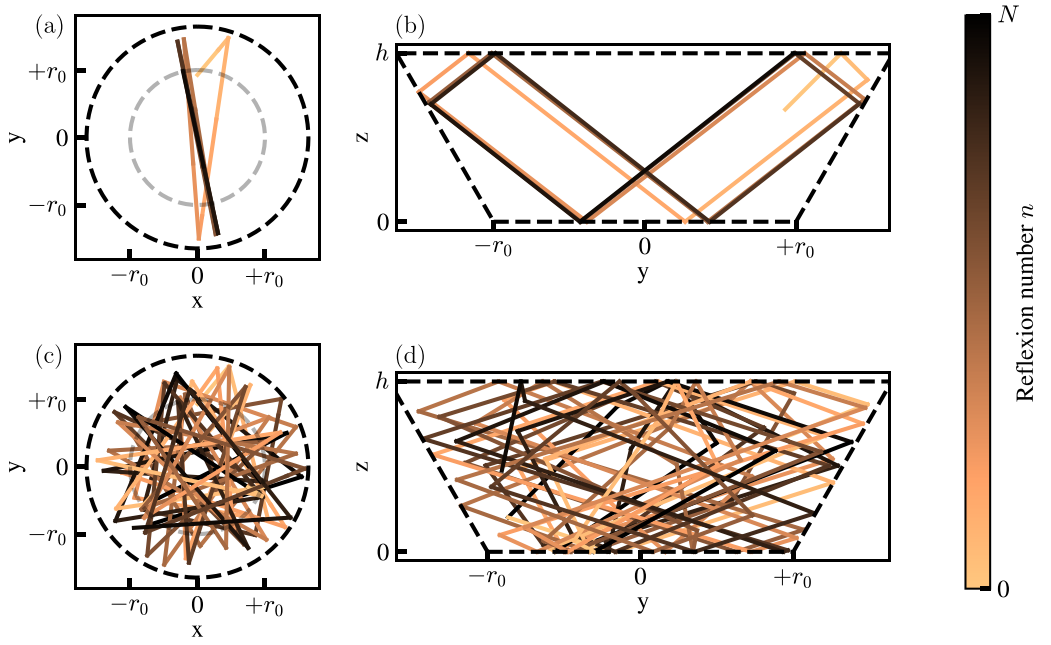

FIG. 5. (a) Horizontal plane projection of a trajectory in 3D space for an inertia-gravity wave with $\sin\theta_0 = 0.61$ inside the experimental setup computed by a ray tracing algorithm with $N = 20$ reflections. The gray dashed line is the bottom base circle; the black dashed line is the top base circle. (b) Vertical projection of the same trajectory. (c) Same as (a) for $\sin\theta_0 = 0.292$ and $N = 100$. (d) Vertical projection.

convergence, and black pixels correspond to parameters for which the convergence is slow or where there is no convergence. The two bright zones where the convergence is the fastest are exactly the same as the ones described for the 2D attractor formation, and similarly the other bands correspond to the smaller Arnold tongues of Fig. 3, which has been reproduced in Fig. 7(a). It appears from this comparison that there is a coupled mechanism for convergence both in the horizontal plane and in the vertical plane. The flaw in the previous description is to consider only focusing reflections when $v_z < 0$ at the reflection leading to $\gamma_\phi < 1$. In the case $v_z > 0$, the reflection is defocusing ($\gamma_\phi > 1$), not leading to convergence in the xy plane, with limit cycles or chaotic-like behavior as shown in Fig. 5(c) and Fig. 5(d). The formation of an attractor in the xz plane ensures focusing reflections on the slope and so convergence in the two planes.

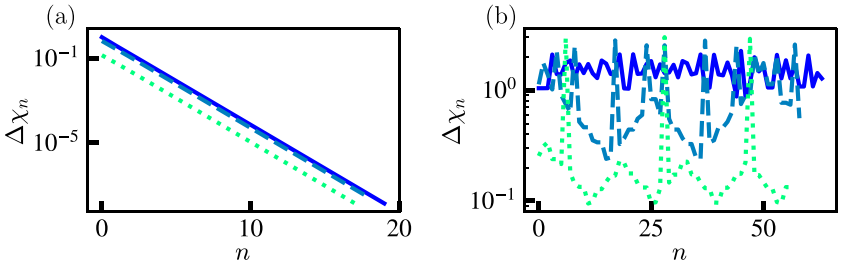

FIG. 6. (a) Semilogarithmic evolution of the azimuthal angle difference $\chi_n^r - \chi_n^i$ as a function of the reflection number n for $\sin\theta = 0.61$ and three different initial angles ϕ_0 (0° line; 40° dashed, and 80° dotted). (b) Same plot with $\sin\theta = 0.292$.

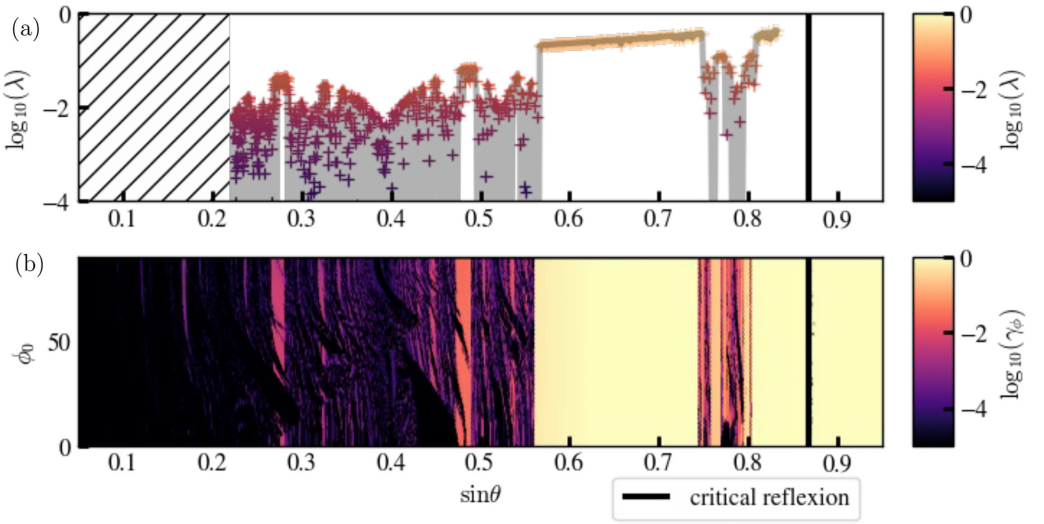

FIG. 7. (a) Reproduction of Fig. 3(b), values of the Lyapunov exponent in the 2D case as a function of $\sin\theta$. Crosses are the numerical points colored according the value of $\log\lambda$. The hatched region corresponds to values of $\tau > 6$ not computed, and the black line corresponds to the critical reflection $\theta = \alpha$. (b) Value of $\log\Lambda_\phi$ as a function of $(\phi_0, \sin\theta)$.

This result implies that the predictions of the 2D model are useful to tailor the formation of an attractor: if a wave is forced at ω_0 such that $\sin\theta$ is in the (1,1) or the (2,1) regions, we expect an attractor to form in every vertical plane, forming a 3D structure invariant under rotation. Yet this structure is not a true localized attractor in the mathematical sense as all initial conditions do not lead to the same limit cycle [19], but a continuous collection of 2D attractors.

III. RESULTS

A. Formation of attractors

Using the previous model, we forced a linearly stratified fluid with $N = 0.76 \pm 0.05\,\mathrm{rads}^{-1}$ without rotating the tank ($f_c = 0$), choosing $T_0 = 2\pi/\omega_0 = 12.93\,\mathrm{s}$ so that $\sin\theta_0 = 0.64$ lies in the middle of the (1,1) region (experiment E in Table I). Let us first consider a linear attractor formation by forcing at small amplitudes, i.e., $a_0 = 1\,\mathrm{mm}$. Figure 8 shows v_x along a period of forcing at relative phases 0, $\pi/2$, π and $3\pi/2$, in a vertical cut through the center of the tank after around $100T_0$ of forcing, after the stationary regime is well established. The velocity field is composed of two usual trapezoidal (1,1) attractors that are classically observed in two dimensions. The observed structure, overlapping with the limit cycle computed by the 2D ray-tracing algorithm, confirms the insights of the numerical analysis. The numeric limit cycle has been displayed with a value of $\sin\theta_{\mathrm{exp}} = 0.622$ fitted to maximize the overlap with the kinetic energy $e_c = (v_x^2 + v_z^2)/2$ averaged over one period of forcing. The relative difference $(\theta_{\mathrm{exp}} - \theta_0)/\theta_0 = 3.5\%$ indicates a good agreement within error bars mainly due to the measure of N.

The main difference with [43] is the interaction at the center, which can be seen both as a reflection on the rotation axis or a wave crossing with an increase of the velocity amplitude from the sides to the center, which is expected with energy conservation as they are cylindrical waves. Also, a node on the axis of reflection is present in this regime. An increase in the velocity amplitude is also observed at the reflections on the slope which was already the case in two dimensions, and theoretically expected from the reflection law.

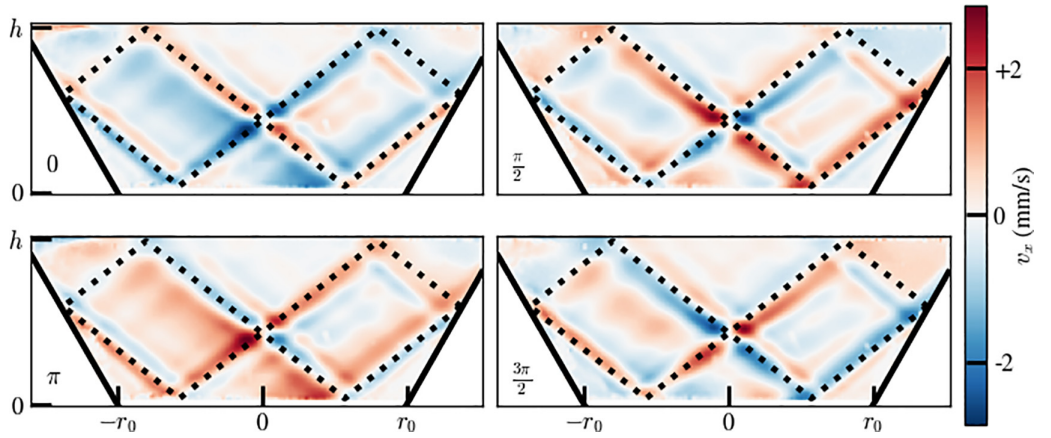

FIG. 8. Snapshots of v_x field, in a vertical cut through the center of the tank after around $100T_0$ of forcing for an internal gravity wave $f_c = 0$ (experiment E in Table I, with $\sin\theta_0 = 0.64$).The velocity filed is filtered around the forcing frequency with a window $0.05\,N$ wide. In the lower left corner is indicated the relative phase to the first snapshot. The thick lines are, respectively, the boundaries of the inner tank (the cone). The dotted thick black line is the limit cycle computed with the 2D ray-tracing algorithm using the best fit to the kinetic energy.

Horizontal views in Fig. 9 of the velocity field filtered around the forcing frequency for an inertial wave (experiment B in Table I) show that this structure is 2π-periodic, following the periodicity of the forcing corresponding to an azimuthal number of -1. Each row is a cut at height $z = 15\,\text{cm}$, 20 cm, and 25 cm from bottom to top. v_r and v_φ have a phase difference of $\pi/2$ as expected. The 3D structure is a continuously phase-shifted 2D attractor. The reflection on the rotation axis is located around $z = 20\,\text{cm}$. The direction of the spiral is given by the phase velocity, which is inward if $z > 20\,\text{cm}$ and outward when $z < 20\,\text{cm}$; those structures all rotate clockwise following the forcing in the stationary regime.

B. Linear response function

One way to characterize the system in the linear regime is to look at the response function to an impulse. The closest forcing to an impulse in our setup is one cosine oscillation in 5 s with amplitude $a_0 = 10\,\text{mm}$, injecting a significant proportion of energy in the range of frequencies of interest. The velocity field is then recorded for 5 min. The experiment was done for both a stratified fluid without rotation (experiment G in Table I) and a rotating homogeneous fluid (experiment D in Table I). The linear response function of the system or transfer function is the output, the power spectral density

$$\tilde{e}_c = \frac{\langle \tilde{v}_x^2 \rangle + \langle \tilde{v}_z^2 \rangle}{2}, \tag{10}$$

divided by the input, the squared velocity of the plate $(\omega\tilde{a})^2$. This quantity is represented in Fig. 10(a) for the stratified nonrotating fluid (N *case*: $N \neq 0$ and $f_c = 0$) and in Fig. 10(b) for the homogeneous rotating fluid (f_c *case*: $N = 0$ and $f_c \neq 0$) with a retrograde forcing.

In both cases, the response of the system is not smooth as peaks are present in the system. The peaks have been characterized by filtering the velocity field around those frequencies as shown in Fig. 10(c). Two different classes can be clearly distinguished, standing waves that resonate in the tank [middle and right columns of Fig. 10(c), in red for the N *case* and blue for the f_c *case*] and attractors [left column of Fig. 10(c), in green, observed only in the N *case*]. The peak at $\omega/f_c = 0.26$ is not shown here and corresponds to a seiche mode in a privileged direction.

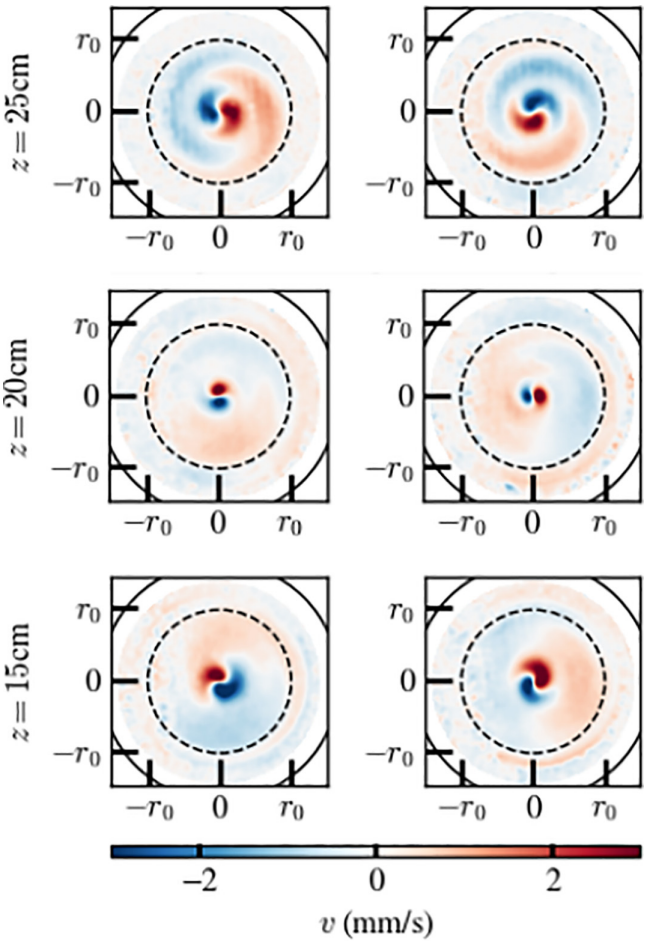

FIG. 9. Horizontal views with a laser sheet at height $z = 25$ cm, 20 cm, and 15 cm from top to bottom, showing v_r (left) and v_φ (right). In this experiment $N = 0$, $f_c = -1.05\,\mathrm{rads}^{-1}$ (experiment B in Table I) and $\omega_0/f_c = 0.767$. The velocity field is filtered around the forcing frequency with a window $0.05 f_c$ wide.

1. The modes

The resonant modes are standing waves due to the presence of the tank boundaries and are presented in increasing mode number from top to bottom in Fig. 10(c). In a attempt to describe those standing waves, we will make a first approximation, that in the z direction k_z can be written as

$$k_{z,n} = n\frac{\pi}{h}, \qquad \text{with } n \in \mathbb{N}^*, \tag{11}$$

similar to any wave trapped between two nodes distant of h. In the radial direction, a Bessel function is adapted to the axisymmetric geometry such that

$$v_x(r, \theta, z) = a \cos(k_z z) J_0(k_r r), \tag{12}$$

k_r being defined by the first zero of the Bessel function $k_r R \simeq 2.4$. The geometry being a cone and not a cylinder, the choice of R is arbitrary, so we considered it to be between the two radii r_0 and R_h of the bases of the frustum. This first approximation gives good results for inertial waves but is not convincing for internal gravity waves. We will therefore use the more complete description

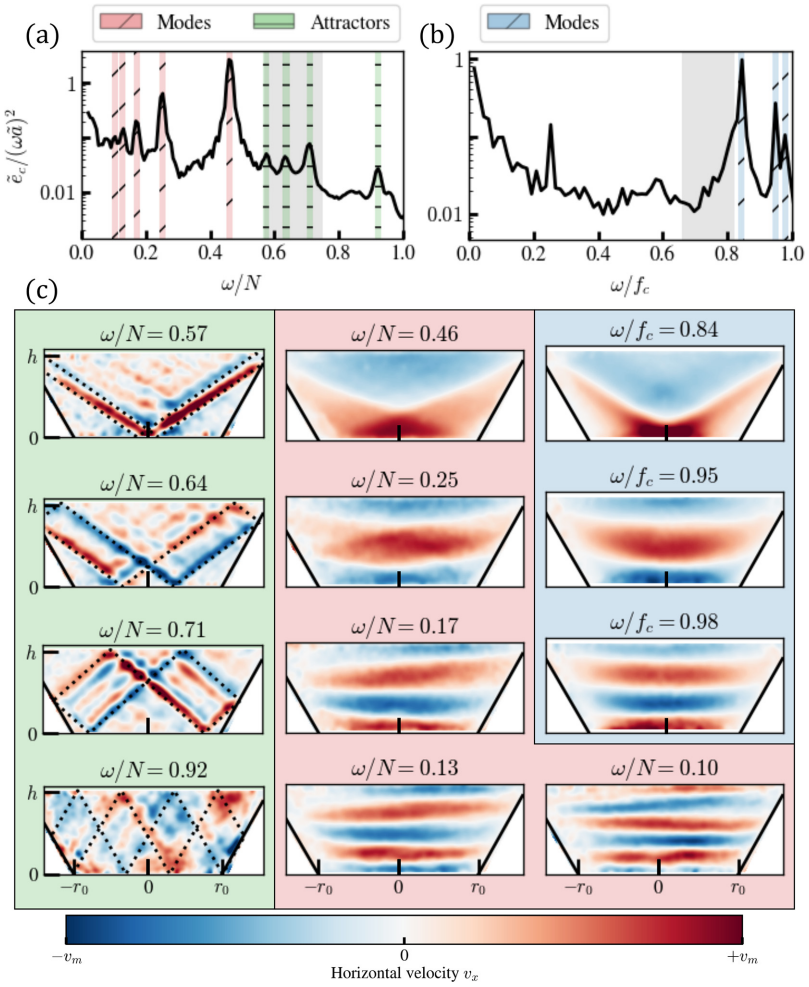

FIG. 10. (a, b) Linear response function $\tilde{e}_c/(\omega\tilde{a})^2$ of the system, in the *N case* (experiment G in Table I) (a) and the f_c *case* (experiment D in Table I) (b). The gray region is the (1,1) Arnold tongue. (c) Snapshots of the velocity field v_x at attractor frequencies (green, left), standing waves frequencies in the *N case* (red, middle), and mode frequencies in the f_c *case*. The filtered frequency is indicated above each snapshot and is represented with the corresponding colors in (a) and (b). The peak at $\omega/f_c = 0.26$ in (b) is a seiche mode in a privileged direction due to the forcing. The color scale has been normalized and centered independently for each snapshot. The values of v_m are given in mm/s: (first row) 0.2, 1, 1.25; (second row) 0.2, 0.6, 1; (third row) 0.3, 0.4, 0.6; (fourth row) 0.15, 0.2, 0.15.

of inertia-gravity waves in a cylindrical confined geometry [44]. The calculation assumes for v_z an axisymmetric mode $m = 1$ in the azimuthal direction with amplitude $v_{z,0}$:

$$v_r(r,z,\theta,t) = i\frac{k_z v_{z,0}}{4k_r\omega}[(f_c - 2\omega)\mathrm{J}_0(k_r r) + (f_c + 2\omega)\mathrm{J}_2(k_r r)]e^{i(\omega t - k_{z,n} z - \theta)} + \text{c.c.}, \tag{13}$$

$$v_z(r,z,\theta,t) = v_{z,0}\mathrm{J}_1(k_r r)e^{i(\omega t - k_{z,n} z - \theta)} + \text{c.c.} \tag{14}$$

The impermeability condition is

$$\vec{v}\cdot\vec{n} = v_z(R(z))\sin\alpha - v_r(R(z))\cos\alpha = 0, \tag{15}$$

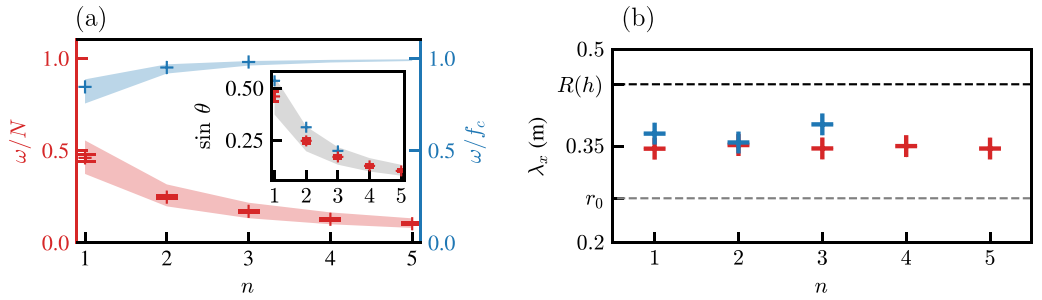

FIG. 11. (a) Measure of the frequency of mode number n. Points are experimental data, in red for the N *case* and in blue for the f_c *case*. Colored regions are the predicted spans of the model. (b) Radial wavelength deduced from the experiments, the dashed lines are the diameter (r_0, R) of the two bases of the frustum.

where $R(z)$ is the radius of the frustum at height z. k_r is defined by the first zero of this sum of Bessel functions, which is denoted by ζ, i.e., $k_r = \zeta/R$. Since the geometry is not cylindrical but frustoconical, the choice of R is arbitrary and can reasonably be chosen between r_0 and R_h, the radii of the two bases of the frustum. By inserting the dispersion relation for internal gravity waves or inertial waves, the model predicts the frequencies at which these standing waves should be found. For internal gravity waves it gives

$$\frac{\omega_n^2}{N^2} = \sin^2\theta = \frac{k_r^2}{k_r^2 + k_{z,n}^2} = \frac{1}{1 + \left(\frac{\pi}{h}\frac{R}{\zeta}\right)^2 n^2}, \tag{16}$$

and for inertial waves

$$\frac{\omega_n^2}{f_c^2} = \cos^2\theta = \frac{k_{z,n}^2}{k_r^2 + k_{z,n}^2} = \frac{n^2}{n^2 + \left(\frac{h}{\pi}\frac{\zeta}{R}\right)^2}. \tag{17}$$

The expressions (13) and (14) are out of phase by $\pi/2$, so the impenetrability condition can be verified only if $v_r(R) = 0$ and $v_z(R) = 0$. The first one leads to $\zeta = 1.84$ for internal gravity waves and $\zeta = 1.33$ for inertial waves, the second to $\zeta = 3.8$ in both cases. The two relationships (16) and (17) correspond to the two colored regions in Fig. 11(a), in red for the N *case* and blue for the f_c *case*. The experimental points are obtained from the location of the peaks in the power spectral density. The model, represented by the color span, shows good agreement by taking $\zeta = 1.84$ for the internal gravity waves. In the other case, the agreement is bad, and we used $\zeta = 2.4$, the first zero of the Bessel function J_0, the first approximation we made. The dispersion relation for inertia-gravity waves makes it possible to unify the two descriptions, as shown in the insert. Another way of comparing the experimental results and the model is to invert the relationship (16) to deduce an effective radius of the cylinder at each frequency peak corresponding to the Bessel function of the n mode. In Fig. 11(b) these effective diameters are well within the radii of the cone bases.

This model is still an approximation, taking the solutions and the boundary conditions for a cylinder, but still helps to describe the peaks in the linear response function.

The shape of the mode $n = 1$ differs strongly from one that could be expected in a cylinder. Being the mode with the largest vertical wavelength, it is expected to be more affected by the effect of the slope. Another explanation could be the vicinity of the $n = 1$ mode's frequency to the boundary of the (1,1) attractor region, especially in the f_c *case*, the attractor consisting of a line between an high corner of the cone and the center of the bottom base [the first snapshot in Fig. 10(c) is an example]. The description seems to hold in this case.

2. The attractors

In Fig. 10 the gray region is the (1,1) Arnold tongue of Fig. 3 and Fig. 7(b), which encompasses as expected the (1,1) attractor pictured in green in Fig. 5(c). In the *N case*, the energy in this region is high with a clear-cut at the region boundary $\omega/N = 0.75$ while being an order of magnitude smaller than the $n = 1$ modes. The fourth peak ($\omega/N = 0.92$) is a noisier (2,1) attractor. On the attractors of Fig. 10(c), the ray-tracing algorithm at the corresponding frequency has been superimposed. In the f_c *case* [Fig. 10(b)], the influence of the attractors is less clear, and the only clue is the asymmetry of the $n = 1$ mode's peak at $\omega/f_c = 0.84$.

Finally, one can remark that the mode description for the *N case*, the f_c *case*, or even intermediate cases is the same using the dispersion relation

$$\sin\theta = \sqrt{\frac{\omega^2 - f_c^2}{N^2 - f_c^2}}, \tag{18}$$

as shown in the inset of Fig. 11(a). It is still important to note that for inertia-gravity waves, the attractor regions that can be seen experimentally have frequencies higher than the standing waves observed if $N > f_c$ (a behavior close to internal gravity waves) but lower frequencies in the case $f_c > N$ (a behavior closer to inertial waves).

C. Weakly nonlinear regime

1. Global picture

In experiments with sinusoidal forcing at moderate amplitude a_0 ranging from 3 mm to 6 mm, there is a spontaneous generation of two secondary waves with frequencies ω_1 and ω_2 smaller than the forcing frequency ω_0, characterized by peaks in the power density spectra. Such a spectrum is displayed in Fig. 12(a) and Fig. 13(b), for an experiment with nonrotating stratified fluid (experiment E in Table I) with a window of $120T_0$ centered around $T = 340T_0$ and averaged spatially over the whole domain. This spectrum shows that $\omega_0 = 0.64 \pm 0.01\,N$, $\omega_1 = 0.22 \pm 0.01N$, and $\omega_2 = 0.43 \pm 0.01N$. Those frequencies satisfy the relation $\omega_0 = \omega_1 + \omega_2$, the temporal resonance condition of the triadic resonance instability (TRI). The amplitude of internal gravity waves on the attractor corresponding to the chosen forcing frequency is high enough to trigger nonlinear effects and especially TRI, generating so-called subharmonics. On this point, we recover the same results as previously obtained in 2D tanks [45]. Looking at the energy transfer efficiency, the ratio $\tilde{e}_c(\omega_1)/\tilde{e}_c(\omega_0)$ is of order 0.05, similar to other studies [43,46], synonymous of a weak energy transfer.

2. Rotation and stratification

The description made previously holds for internal gravity waves ($f_c = 0$, *N case*) sufficiently forced, but differences are observed even in the qualitative description of the TRI in the case of homogeneous rotating fluid (f_c *case*, inertial). For inertial waves, the energy transfer is even weaker, and no clear peak can be distinguished.

Figure 12(a) displays the time-frequency diagram corresponding of an internal gravity wave (*N case*) experiment, with $a_0 = 3$ mm and frequency $\omega_0/N = 0.64$. For each time t the power density spectrum $\tilde{e}_c$ is computed from the Fourier transform of the velocity field with a window of width $120T_0$, averaged spatially over the whole domain. The cumulative power density spectrum is represented on the right. Figures 13(a) and 13(b) are cuts around, respectively, $t = 80T_0$ and $340T_0$ of this diagram indicated by white dashed lines in Fig. 12(a). Correspondingly, in Fig. 12(b) is represented the time-frequency diagram for an experiment with inertial waves with forcing amplitude $a_0 = 3$ mm and frequency $\omega_0/f_c = 0.768$ such that $\sin\theta = \sqrt{1 - (\omega_0/f_c)^2} = 0.64$, thus creating the same attractor. Figures 13(c) and 13(d) are cuts around, respectively, $t = 60T_0$ and $110T_0$. Note that Fig. 12(a) and Fig. 12(b) have a different color scale.

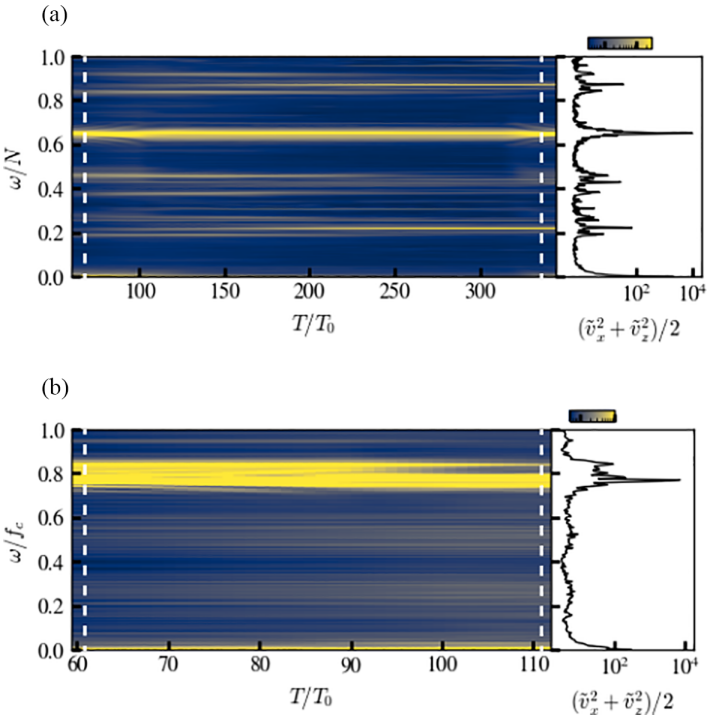

FIG. 12. (a, b) Time-frequency diagram with a window of $120T_0$ for experiments with $a_0 = 3\,\text{mm}$, $\sin\theta = 0.64$, and, respectively, $(N, f_c) = (0.77, 0)\,\text{rads}^{-1}$ (*N case*, experiment E in Table I) and $(N, f_c) = (0, 1.05)\,\text{rads}^{-1}$ (f_c *case*, (experiment B in Table I)). The white dashed lines are placed at $t = t_{\max}/10$ and $9t_{\max}/10$. Note that (a) and (b) have a different color scale, whose range is indicated above the spectra.

In comparison to the description of Fig. 13(b), differences are observed in Fig. 13(d) in the f_c *case*(experiment B in Table I): instead of two sharp peaks, a wider range is observed for the couple (ω_1, ω_2), forming two wide peaks, coherent with observation made by [47,48]. It can also be noted that the energy transfer is weaker. The time evolution between Fig. 13(c) and Fig. 13(d) shows a slight increase of the energy at the forcing and the subharmonic frequencies, whereas the peak at $\omega = \omega_{n=1} = (0.85 \pm 0.01)f_c$, which is the first resonant mode, decreases, indicating that it has been generated at the start of the experiment.

The filtered velocity field at ω_1 and ω_2 for both cases represented in Fig. 14 shows very different patterns for internal gravity waves (a and b) and inertial waves (c and d). The amplitude of the subharmonics of inertial waves is larger near the center and decays radially both because of viscosity and the cylindrical geometry. Experiments with inertial waves did not show as clear structures as internal gravity waves when TRI is involved, so an experiment has been made with cameras placed closer to get a better spatial resolution. This could indicate generation of the waves at the center of the tank where the amplitude of the forcing attractor is the largest.

The internal gravity wave subharmonic shows clearly a mode resonating in the tank; it would be described by a mode number $n = 4$ according to the numbering of Sec. III B and an azimuthal number $m = 0$ described better by a Bessel function of order 1, the difference with Sec. III B being the symmetry around the rotating axis. The main frequency selection mechanism for the subharmonics is not the growth rate but the resonance with the tank for at least one of ω_1 and ω_2. The specificity of the internal gravity waves is encoded in their linear response function, where it is clear in Fig. 10 that the attractor frequency span is above the resonant modes frequencies as opposed to inertial waves for which the resonant modes lie close to f_c. Therefore TRI, which excites

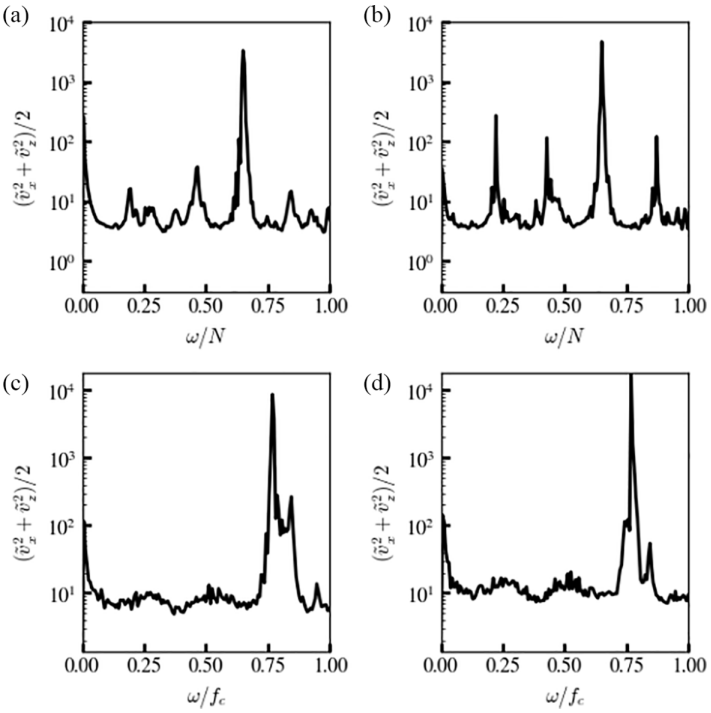

FIG. 13. (a, b) Power density spectra of the kinetic energy in the *N case* at $t = t_{\max}/10$ and $9t_{\max}/10$ with window $120T_0$, corresponding to vertical slices of Fig. 12(a). (c, d) The equivalent for Fig. 12(b) in the f_c *case*.

lower frequencies, can produce resonant, peaked modes for the internal gravity waves and not in the inertial waves case where the frequency selection reflects the growth rate of the instability. A recent study [49] showed that inhibiting the modes in the internal gravity waves makes the behavior of the TRI closer to the inertial case. Also, in the case of inertial waves, some energy can be transferred to the geostrophic mode when the forcing amplitude is high enough, which in return shifts the frequencies of the daughter waves, inhibiting TRI [30].

In the internal gravity wave time-frequency diagram presented in Fig. 12(a), the dominant subharmonic couple is not the same at the beginning and the end of the experiment, which is clear comparing Figs. 13(a) and 13(b), explaining the presence of more subharmonics in the cumulative spectrum than in Fig. 13(b) [50]. The mode structure is less clear when filtering the velocity field at the two other possible subharmonic frequencies $\omega_1' = 0.19$ and $\omega_1'' = 0.26$. At the beginning, the amplitude of the peak at $\omega_1' = 0.19$ is bigger, suggesting a higher growth rate, while at the end, the peak at $\omega_1 = 0.22$ is dominant. The resonant mode has a lower growth rate but accumulates energy over time, increasing its interaction term with the forcing wave until it becomes the predominant triad for TRI.

D. Axis dissipation

TRI is a robust phenomenon constituting a first step toward energy transfer between scales. With hope to obtain a continuous spectrum close to a weak wave turbulence regime, the amplitude a_0 has been increased up to 10 mm. It has been shown in two dimensions [27,46] that TRI could build the spectrum by successive triadic interactions, which is not observed in our experiments as, at most, two TRI steps have been reported. Actually, observations tend to show the opposite: an increase in the forcing amplitude past the TRI threshold is associated with an increase of the width of the attractor and especially an increase in the wavelength, and subharmonics disappear from the power spectral density. Furthermore, the overall structure of the attractor is lost as the amplitude is

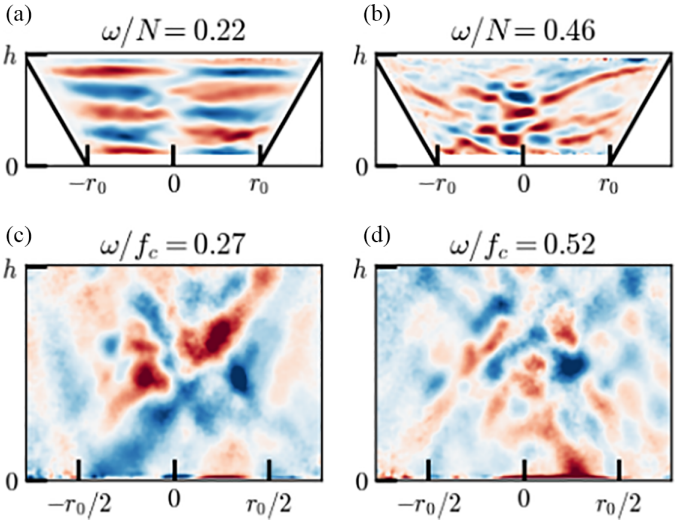

FIG. 14. Snapshots of the velocity field v_x. (a, b) For the *N case*, filtered at $\omega_1/N = 0.22$ (a), $\omega_1/N = 0.46$(b), the subharmonics for internal gravity waves. (c, d) For the f_c *case*, filtered at $\omega_1/f_c = 0.27$ (c), $\omega_2/f_c = 0.46$(d), the subharmonics for inertial waves.

increased. These two phenomena were not observed in the 2D case, leading us to point as the main factor for the differences to the interaction on the symmetry axis where the amplitude of the velocity field is maximum.

To investigate the effect of the rotation axis reflection, a solid cylinder is placed at the center of the tank preventing the divergence of the amplitude at the axis and the interaction of waves coming from all directions. Two different cylinders have been used, of respective diameters $d = 2$ cm and 11 cm, in order to probe the characteristic length of the axis interaction. All experiments have been conducted with inertial waves of parameter $f_c = 1.05\,\text{rads}^{-1}$ (experiment E in Table I), forcing amplitudes a_0 of 1 mm and 2 mm, respectively, and $\sqrt{1-(\omega_0/f_c)^2}$ of 0.75 and 0.69, respectively, to keep the forcing frequency in the middle of the (1,1) Arnold tongue as the geometry changes. Figure 15 represents the x-velocity field filtered at their respective forcing frequency with the same frequency span $\delta\omega/f_c$ of 0.05. Qualitatively, the width of the attractor beams decreases when the diameter goes from 2 cm to 11 cm and the wavelength of the wave inside the attractor envelope decreases. Usually in 2D attractor experiments, the width of an attractor is given by the balance between the focusing at the inclined slope and the viscous dissipation along the propagation trajectory [52] and thus should not be influenced by the presence of the cylinder, which is not the case, here underlining the importance of the reflection on the rotation axis.

In 2D experiments, the reflection on the vertical wall is equivalent to the reflections on the horizontal ones [51] as shown in Fig. 15(e). Figure 15(b) shows the kinetic energy e_c averaged over ten periods of forcing. As in two dimensions, there is an increase of the energy at the reflection on the slope, but a difference arises at the reflection on the axis as the interaction zone is wider.

The wide zone of interaction can be seen in Fig. 16(a), showing a vertical cut of the kinetic energy of Fig. 15(b), and in two snapshots with a $\pi/2$ phase difference (dotted and dashed). The region is about 10 cm wide, and the waves propagate in this envelope. Figure 16(b) compares this envelope in the open domain and with a tube at the center. The zone of interaction is bigger in the case without the tube.

Figures 15 and 16 are clues that the reflection on the axis indeed affects the attractor. Experiments with different tube diameter show that the tube has to be large enough, approximately 10 cm in diameter, for the differences to be clear.

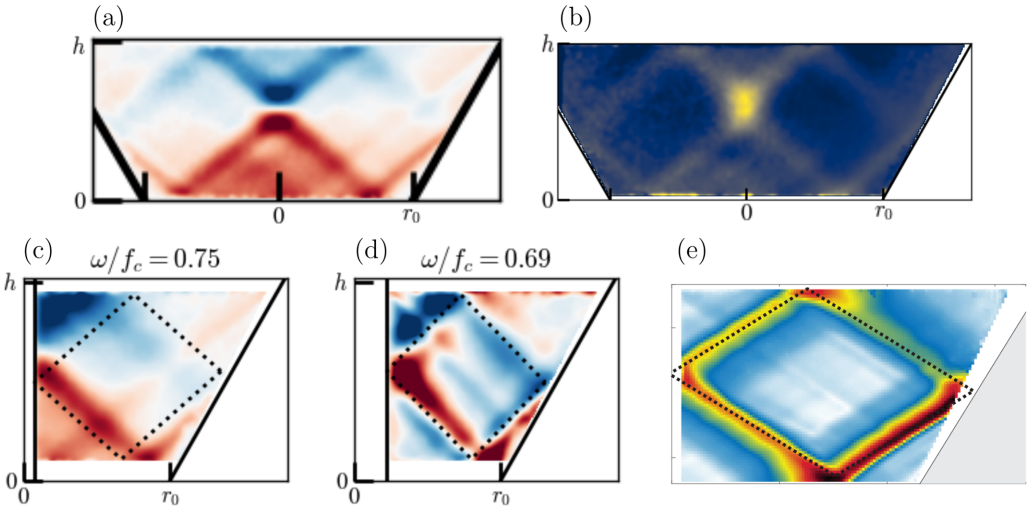

FIG. 15. Snapshot of v_x in an homogeneous fluid in rotation with $f_c = -1.05\,\mathrm{rads}^{-1}$ (experiment B in Table I), without cylinder (a), and the corresponding kinetic energy e_c averaged over $10T_0$ (b). A cylinder has been placed at the center with a diameter d of 2 cm (c) and 11 cm (d). The velocity is filtered around their respective forcing frequency with $\delta\omega = 0.05 f_c$. (e) Kinetic energy averaged over T_0 in an experiment with internal gravity waves in the 2D case, extracted from [51].

IV. CONCLUSION

Through laboratory experiments and ray tracing algorithm, the present study displays some properties of inertia-gravity waves in an axisymmetric 3D tank. The inclined slope of the frustum induces a convergence in the vertical plane [a 2D-(m, n) attractor of the trapezoid], while the circular shape and the 3D properties of reflection of inertia-gravity waves ensure the convergence in the horizontal plane (in a diameter). In the right frequency span, a coupled convergence leads any trajectory to a limit cycle, an attractor. In the (1,1) convergence zone, the attractor is actually a collection of 2D-(1,1) attractors organized around as a rhombus shaped torus. Experimental

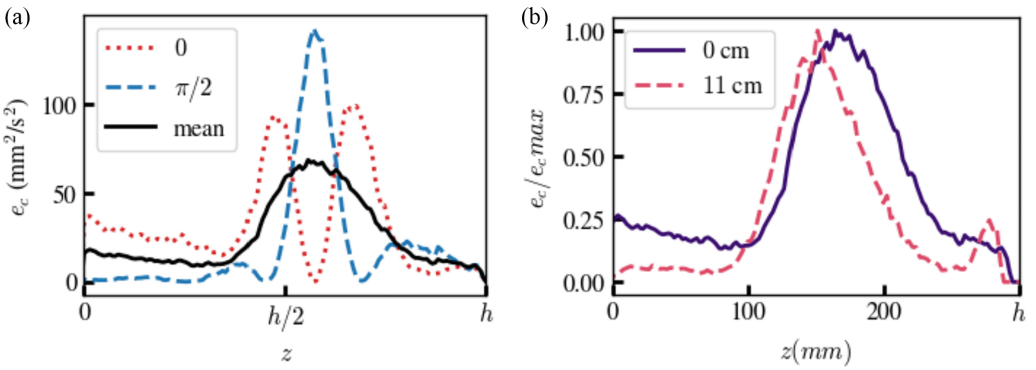

FIG. 16. (a) Profile along a vertical cut, of the kinetic energy e_c for an inertial wave experiment with $f_c = -1.05\,\mathrm{rads}^{-1}$, 1 cm away from the middle of the tank. The dotted line and the dashed line are instantaneous profiles with a relative phase shift of $\pi/2$ in the stationary regime. The solid line is the mean profile over $50T_0$. (b) Profile along a vertical cut, of the normalized mean kinetic energy $e_c/e_{c,\max}$ for the situation without a tube (solid) and with an 11 cm tube (dashed).

observations of such structures have been made, for inertial, internal gravity, and inertia-gravity waves. In the linear regime, the attractor is a continuous 3D structure, where each cross section is a 2D attractor whose phase follows the $m = -1$ azimuthal wave number of the forcing.

An impulse experiment reveals experimentally the zones of attractors and the existence of standing waves that are easily excited. Constant amplitude experiments at larger amplitude induce triadic resonance instability (TRI), due to the focusing of the energy by the attractor and the convergence to the center of the tank. This well-known and well-studied instability [10] triggers differently internal gravity waves and inertial waves. On the one hand, for internal gravity waves, one of the daughter waves is an easily excited standing wave. On the other hand, for inertial waves, the standing waves cannot be excited as their frequency is above the (1,1) Arnold tongue.

The mechanism of interaction on the axis of symmetry remains open. Experiments suggest that the convergence on this point triggers mixing and destroys the structure of the attractor for internal gravity waves. The loss of structure is also reported for inertial waves at large forcing amplitudes. Yet at small amplitudes, a behavior closer to the 2D case can be retrieved by adding a cylinder of sufficient diameter at the center of the domain for the wave to reflect on. The main mechanism is the widening of the convergence zone with larger velocities.

Contrary to a previous study in the 2D case [27], no wave turbulence has been observed nor a cascade of TRI. The energy is dissipated through wave interactions only at medium amplitude, but through turbulence and wave breaking at the center at large amplitudes.

ACKNOWLEDGMENTS

The authors acknowledge support from the Simons Foundation through Grant No. 651475. The experiments performed in Lyon were supported by LABEX iMUST (ANR-10-LABX-0064) of the Université de Lyon, within the program "Investissements d'Avenir" (ANR-11-IDEX0007), and by DisET (ANR-17-CE30-0003), operated by the French National Research Agency (ANR). Experimental analyses were achieved thanks to the resources of PSMN from ENS de Lyon. E.E. thanks ENS de Lyon and CNRS for visiting professorship invitations.

[1] J. A. MacKinnon, Z. Zhao, C. B. Whalen, A. F. Waterhouse, D. S. Trossman, O. M. Sun, L. C. St. Laurent, H. L. Simmons, K. Polzin, R. Pinkel *et al.*, Climate process team on internal wave–driven ocean mixing, Bull. Am. Meteorol. Soc. **98**, 2429 (2017).

[2] K. L. Polzin, An abyssal recipe, Ocean Model. **30**, 298 (2009).

[3] C. de Lavergne, S. Falahat, G. Madec, F. Roquet, J. Nycander, and C. Vic, Toward global maps of internal tide energy sinks, Ocean Model. **137**, 52 (2019).

[4] C. Wunsch and R. Ferrari, Vertical mixing, energy, and the general circulation of the oceans, Annu. Rev. Fluid Mech. **36**, 281 (2004).

[5] O. Bühler and M. Holmes-Cerfon, Decay of an internal tide due to random topography in the ocean, J. Fluid Mech. **678**, 271 (2011).

[6] W. H. Munk, Abyssal recipes, Deep Sea Res. Oceanogr. Abs. **13**, 707 (1966).

[7] F. Pollmann, Global characterization of the ocean's internal wave spectrum, J. Phys. Oceanogr. **50**, 1871 (2020).

[8] C. Garrett, Internal tides and ocean mixing, Science **301**, 1858 (2003).

[9] S. Cole, D. Rudnick, B. Hodges, and J. Martin, Observations of tidal internal wave beams at Kauai Channel, Hawaii, J. Phys. Oceanogr. **39**, 421 (2009).

[10] T. Dauxois, S. Joubaud, P. Odier, and A. Venaille, Instabilities of internal gravity wave beams, Annu. Rev. Fluid Mech. **50**, 131 (2018).

[11] O. M. Phillips, *The Dynamics of the Upper Ocean* (Cambridge University Press, Cambridge, 1966).

[12] L. Gostiaux, T. Dauxois, H. Didelle, J. Sommeria, and S. Viboud, Quantitative laboratory observations of internal wave reflection on ascending slopes, Phys. Fluids **18**, 056602 (2006).
[13] R. H. Nazarian and S. Legg, Internal wave scattering in continental slope canyons, part 1: Theory and development of a ray tracing algorithm, Ocean Model. **118**, 1 (2017).
[14] L. R. Maas and F.-P. A. Lam, Geometric focusing of internal waves, J. Fluid Mech. **300**, 1 (1995).
[15] L. R. Maas, D. Benielli, J. Sommeria, and F.-P. A. Lam, Observation of an internal wave attractor in a confined, stably stratified fluid, Nature (London) **388**, 557 (1997).
[16] N. Grisouard, C. Staquet, and I. Pairaud, Numerical simulation of a two-dimensional internal wave attractor, J. Fluid Mech. **614**, 1 (2008).
[17] M. Brunet, T. Dauxois, and P.-P. Cortet, Linear and nonlinear regimes of an inertial wave attractor, Phys. Rev. Fluids **4**, 034801 (2019).
[18] G. Pillet, E. Ermanyuk, L. Maas, I. Sibgatullin, and T. Dauxois, Internal wave attractors in three-dimensional geometries: Trapping by oblique reflection, J. Fluid Mech. **845**, 203 (2018).
[19] B. Favier and S. Le Dizes, Inertial wave super-attractor in a truncated elliptical cone (unpublished).
[20] M. Rieutord, B. Georgeot, and L. Valdettaro, Inertial waves in a rotating spherical shell: Attractors and asymptotic spectrum, J. Fluid Mech. **435**, 103 (2001).
[21] B. Dintrans, M. Rieutord, and L. Valdettaro, Gravito-inertial waves in a rotating stratified sphere or spherical shell, J. Fluid Mech. **398**, 271 (1999).
[22] J. He, B. Favier, M. Rieutord, and S. Le Dizès, Internal shear layers in librating spherical shells: The case of periodic characteristic paths, J. Fluid Mech. **939**, A3 (2022).
[23] W. Tang and T. Peacock, Lagrangian coherent structures and internal wave attractors, Chaos **20**, 017508 (2010).
[24] P. Echeverri, T. Yokossi, N. Balmforth, and T. Peacock, Tidally generated internal-wave attractors between double ridges, J. Fluid Mech. **669**, 354 (2011).
[25] Y. Guo and M. Holmes-Cerfon, Internal wave attractors over random, small-amplitude topography, J. Fluid Mech. **787**, 148 (2016).
[26] S. Nazarenko, *Wave Turbulence*, Lecture Notes in Physics Vol. 825 (Springer-Verlag, Berlin, Heidelberg, 2011).
[27] G. Davis, T. Jamin, J. Deleuze, S. Joubaud, and T. Dauxois, Succession of resonances to achieve internal wave turbulence, Phys. Rev. Lett. **124**, 204502 (2020).
[28] C. Brouzet, I. Sibgatullin, H. Scolan, E. Ermanyuk, and T. Dauxois, Internal wave attractors examined using laboratory experiments and 3D numerical simulations, J. Fluid Mech. **793**, 109 (2016).
[29] E. Yarom and E. Sharon, Experimental observation of steady inertial wave turbulence in deep rotating flows, Nat. Phys. **10**, 510 (2014).
[30] T. Le Reun, B. Favier, and M. Le Bars, Experimental study of the nonlinear saturation of the elliptical instability: Inertial wave turbulence versus geostrophic turbulence, J. Fluid Mech. **879**, 296 (2019).
[31] E. Monsalve, M. Brunet, B. Gallet, and P.-P. Cortet, Quantitative experimental observation of weak inertial-wave turbulence, Phys. Rev. Lett. **125**, 254502 (2020).
[32] C. Rodda, C. Savaro, G. Davis, J. Reneuve, P. Augier, J. Sommeria, T. Valran, S. Viboud, and N. Mordant, Experimental observations of internal wave turbulence transition in a stratified fluid, Phys. Rev. Fluids **7**, 094802 (2022).
[33] M. Klein, T. Seelig, M. V. Kurgansky, A. Ghasemi, I. D. Borcia, A. Will, E. Schaller, C. Egbers, and U. Harlander, Inertial wave excitation and focusing in a liquid bounded by a frustum and a cylinder, J. Fluid Mech. **751**, 255 (2014).
[34] S. Boury, I. Sibgatullin, E. Ermanyuk, N. Shmakova, P. Odier, S. Joubaud, L. R. Maas, and T. Dauxois, Vortex cluster arising from an axisymmetric inertial wave attractor, J. Fluid Mech. **926**, A12 (2021).
[35] R. Beardsley, An experimental study of inertial waves in a closed cone, Stud. Appl. Math. **49**, 187 (1970).
[36] G. A. Henderson and K. D. Aldridge, A finite-element method for inertial waves in a frustum, J. Fluid Mech. **234**, 317 (1992).
[37] B. Bourget, Ondes internes, de l'instabilité au mélange. Approche expérimentale, Ph.D. thesis, École normale supérieure physique Lyon, 2014.

[38] D. Hill, General density gradients in general domains: The "two-tank" method revisited, Exp. Fluids **32**, 434 (2002).
[39] P. Maurer, S. Joubaud, and P. Odier, Generation and stability of inertia–gravity waves, J. Fluid Mech. **808**, 539 (2016).
[40] A. Fincham and G. Delerce, Advanced optimization of correlation imaging velocimetry algorithms, Exp. Fluids **29**, S013 (2000).
[41] A. McEwan, Inertial oscillations in a rotating fluid cylinder, J. Fluid Mech. **40**, 603 (1970).
[42] A. Rabitti and L. R. Maas, Meridional trapping and zonal propagation of inertial waves in a rotating fluid shell, J. Fluid Mech. **729**, 445 (2013).
[43] G. Davis, Attracteurs d'ondes internes de gravité: Des résonances en cascade, Ph.D. thesis, École normale supérieure physique Lyon, 2019.
[44] S. Boury, P. Maurer, S. Joubaud, T. Peacock, and P. Odier, Triadic resonant instability in confined and unconfined axisymmetric geometries, J. Fluid Mech. **957**, A20 (2023).
[45] H. Scolan, E. Ermanyuk, and T. Dauxois, Nonlinear fate of internal wave attractors, Phys. Rev. Lett. **110**, 234501 (2013).
[46] C. Brouzet, E. Ermanyuk, S. Joubaud, I. Sibgatullin, and T. Dauxois, Energy cascade in internal-wave attractors, Europhys. Lett. **113**, 44001 (2016).
[47] G. Bordes, F. Moisy, T. Dauxois, and P.-P. Cortet, Experimental evidence of a triadic resonance of plane inertial waves in a rotating fluid, Phys. Fluids **24**, 014105 (2012).
[48] D. O. Mora, E. Monsalve, M. Brunet, T. Dauxois, and P.-P. Cortet, Three-dimensionality of the triadic resonance instability of a plane inertial wave, Phys. Rev. Fluids **6**, 074801 (2021).
[49] N. Lanchon, D. O. Mora, E. Monsalve, and P.-P. Cortet, Internal wave turbulence in a stratified fluid with and without eigenmodes of the experimental domain, Phys. Rev. Fluids **8**, 054802 (2023).
[50] K. M. Grayson, S. B. Dalziel, and A. G. W. Lawrie, The long view of triadic resonance instability in finite-width internal gravity wave beams, Phys. Rev. Fluids **953**, A22 (2023).
[51] G. Davis, T. Dauxois, T. Jamin, and S. Joubaud, Energy budget in internal wave attractor experiments, J. Fluid Mech. **880**, 743 (2019).
[52] J. Hazewinkel, P. Van Breevoort, S. B. Dalziel, and L. R. Maas, Observations on the wavenumber spectrum and evolution of an internal wave attractor, J. Fluid Mech. **598**, 373 (2008).